Journal of Materials Chemistry A

PAPER

View Article Online
View Journal | View Issue

Published on 16 October 2018. Downloaded by California State University at Long Beach on 6/7/2019 2:09:54 AM.

Check for updates

Cite this: J. Mater. Chem. A, 2018, 6, 22580

In situ synthesis of n–n Bi_2MoO_6 & Bi_2S_3 heterojunctions for highly efficient photocatalytic removal of Cr(VI)†

Xiu-Qing Qiao,[a] Zhen-Wei Zhang,[a] Qiu-Hao Li,[a] Dongfang Hou,[a] Qichun Zhang,[a] Jian Zhang,[a] Dong-Sheng Li,*[a] Pingyun Feng[b] and Xianhui Bu*[c]

Received 27th August 2018
Accepted 14th October 2018

DOI: 10.1039/c8ta08294d

rsc.li/materials-a

Exploiting novel photocatalysts with high efficiency and durability for reduction of hexavalent chromium (Cr(VI)) has gained attention from fundamental science and industrial research. In this work, we synthesized novel two-dimensional (2D) n–n Bi_2MoO_6 & Bi_2S_3 heterojunctions by a facile *in situ* anion exchange process for remarkably efficient removal of Cr(VI). Results show that Bi_2MoO_6 & Bi_2S_3 heterojunctions with core–shell structures are formed through the intimate contact of Bi_2MoO_6 core and Bi_2S_3 shell. The prepared Bi_2MoO_6 & Bi_2S_3 heterojunctions exhibit unprecedented photocatalytic activity for reduction of Cr(VI) under visible light irradiation. The optimized BMO-S1 heterojunction displays the highest reduction efficiency (κ_{app} = 0.164 min^{-1}) for Cr(VI) reduction. To the best of our knowledge, it is one of the highest reduction rate achieved among reported photocatalysts for Cr(VI) reduction under visible-light irradiation. Detailed studies show that strong selective adsorption for Cr(VI) enhances this unprecedented photocatalytic activity. Moreover, the intimate heterojunction between Bi_2MoO_6 core and Bi_2S_3 shell can efficiently deteriorate the charge carrier recombination and Bi_2S_3 content can boost visible light harvesting, thereby contributing to the remarkable photocatalytic catalytic activity, which were proven by PL, EIS and transient photocurrent responses. Characterization of Mott–Schottky plots and DRS prove that the Bi_2MoO_6 & Bi_2S_3 heterojunctions established a type-II band alignment with intimate contact, accounting for the efficient transfer and separation of photogenerated carriers. This work provides a simple route for facial synthesis of heterojunction photocatalysts for Cr(VI) reduction in industrial applications.

1. Introduction

Heavy metal ions, including hexavalent chromium (Cr(VI)), are highly toxic, potentially carcinogenic and non-degradable, thus, posing a serious threat to ecosystems and living organisms.[1,2] As stipulated by the World Health Organization (WHO), the maximum permissible concentration of Cr(VI) in drinking water is 0.05 mg L^{-1}.[3] However, excessive discharge of industrial wastewaters into the environment is far surpassing the limit, which can cause kidney failure, liver cancer, gastric and other damages. Meanwhile, the highly reduced state of Cr(VI), trivalent chromium (Cr(III)), is less toxic and an essential trace element for humans. Accordingly, studies on the high efficiency conversions of Cr(VI) to Cr(III) are rather attractive. During the past few decades, various techniques have been developed to remove Cr(VI) from waste water, including adsorption,[4,5] ion exchange,[6] photocatalytic reduction[2,3] and precipitation methods.[7–9] Among these methods, adsorption is widely studied owing to its low cost and extensive applications.[10] Nevertheless, such methods can only absorb Cr(VI) rather than degrade it and secondary pollution is still a major obstacle. Thus, it is urgent to develop an effective and economical strategy for Cr(VI) reduction. In particular, photocatalytic reduction of Cr(VI) over a semiconductor is emerging as an efficient, green and promising technique since it achieves one-step removal of Cr(VI) by harvesting clean solar energy.[11] During the photocatalytic reduction process, Cr(VI) should first be adsorbed on the surface of catalysts and then, reduced by photo-generated electrons. Therefore, effective adsorption followed by efficient photocatalytic reduction is an efficient, simple and economic method to reduce toxic Cr(VI) to friendly Cr(III). However, to the best of our knowledge, little attention has been paid to the adsorption

[a]College of Materials and Chemical Engineering, Hubei Provincial Collaborative Innovation Center for New Energy Microgrid, Key Laboratory of Inorganic Nonmetallic Crystalline and Energy Conversion Materials, China Three Gorges University, Yichang 443002, PR China. E-mail: lidongsheng1@126.com

[b]Department of Chemistry, University of California, Riverside, CA 92521, USA

[c]Department of Chemistry and Biochemistry, California State University, Long Beach, 1250 Bellflower Boulevard, Long Beach, CA 90840, USA. E-mail: xianhui.bu@csulb.edu

† Electronic supplementary information (ESI) available: EDS of BMO-S1, BET, adsorption performance and UV-vis absorption spectra of all the samples. See DOI: 10.1039/c8ta08294d

This journal is © The Royal Society of Chemistry 2018

Published on 16 October 2018. Downloaded by California State University at Long Beach on 6/7/2019 2:09:54 AM.

performance of Cr(VI) onto a catalyst for the following photocatalytic reduction.[12,13]

Bi_2MoO_6, a Bi-based semiconductor material, has attracted much attention due to its layer structure and good catalytic properties.[14,15] In particular, the suitable bandgap of Bi_2MoO_6 (2.5–2.8 eV) for capturing visible light makes it a potential photocatalyst for water splitting and dye degradation.[16,17] However, the photocatalytic performance of Bi_2MoO_6 is still far from satisfactory because of the rapid recombination of electron–hole pairs after excitation.[18] To suppress the fast recombination of electrons and holes, various significant measures have already been demonstrated, among which construction of Bi_2MoO_6-based heterojunctions with matched energy levels has been proven as one of the most effective strategies. For example, $Bi_2O_2CO_3/Bi_2MoO_6$ heterostructure shows dramatically enhanced visible light photocatalytic degradation of Rhodamine B (RhB) than pure Bi_2MoO_6 and $Bi_2O_2CO_3$, due to the improved charge separation.[18] Bi_2MoO_6/TiO_2 heterostructure exhibits high photocatalytic oxygen production and excellent photodegradation performance under UV and visible light irradiation due to multiple effects, including the matched energy band, improved charge transfer efficiency and suppressed photoelectron–hole recombination.[19] Hierarchical MoS_2/Bi_2MoO_6 composites show significantly enhanced visible light-assisted photocatalytic oxidation of RhB due to improved photo-generated charge separation, more catalytic active sites and light harvesting.[20] Analogously, photocatalytic degradation of RhB over g-C_3N_4/Bi_2MoO_6 heterojunction is enhanced due to the efficient separation of photo-induced electrons and holes.[16] Although the photocatalytic performance of Bi_2MoO_6 was greatly improved, hitherto there has been no report on the application of Bi_2MoO_6 for photocatalytic reduction of Cr(VI).

Additionally, metal sulphides with narrow band gaps, such as Bi_2S_3,[21,22] CdS,[23] MoS_2,[24–26] and WS_2,[27–29] have proven to be effective materials for increased absorption of visible light and adsorption of pollutant molecules. Among them, bismuth sulphide (Bi_2S_3), a well-known lamellar structured semiconductor with a direct band gap of 1.3–1.7 eV, has drawn particular attention for applications in solar cells,[30] photocatalysts,[31] sensors,[32] photodetectors[33] and Schottky diodes.[34] However, the rapid recombination of photo-generated charge carriers in Bi_2S_3 prevents its practical applications. Thus, it is of great significance to construct Bi_2S_3-based heterojunctions with matched energy levels to improve the separation of photo-induced electrons and holes.

It is worth noting that both Bi_2MoO_6 and Bi_2S_3 have the similar layer structure, as well as a common element Bi, which inspired us to construct Bi_2MoO_6 & Bi_2S_3 heterojunctions by a simple *in situ* method. Hence, here, Bi_2MoO_6 & Bi_2S_3 heterojunctions with core–shell structures are prepared by an *in situ* anion exchange method. The Bi_2MoO_6 & Bi_2S_3 heterojunctions exhibit increased surface area, adsorption for Cr(VI) and visible light absorption. Moreover, energy level structure analysis reveals that the matched energy level between Bi_2MoO_6 and Bi_2S_3 can theoretically form type II junction, which enhances the effective separation of electron–hole pairs and their migration between Bi_2MoO_6 and Bi_2S_3, and thus, the photocatalytic activity. Thus, the prepared Bi_2MoO_6 & Bi_2S_3 heterojunctions exhibit remarkable photocatalytic activity, with the efficiency for reduction of Cr(VI) (10 mg L^{-1}) reaching 100% within 15 min under visible light irradiation. To the best of our knowledge, it is one of the best performance among all catalysts for Cr(VI) reduction. The study may advance the use of practical photocatalysts for environmental remediation, and also inspire further development of other such photocatalytic materials.

2. Experimental

All chemicals, including nitric acid (HNO_3), ammonium hydroxide ($NH_3 \cdot H_2O$), bismuth nitrate ($Bi(NO_3)_3 \cdot 5H_2O$), sodium molybdate (Na_2MoO_4), polyvinylpyrrolidone (PVP, M_w = 130 000), sodium sulphide ($Na_2S \cdot 9H_2O$), potassium dichromate ($K_2Cr_2O_7$), Rhodamine B (RhB), methylene blue (MB), methyl orange (MO), acid fuchsin (AF), ciprofloxacin (CIP), and sodium fluorescein (SF) were purchased from Aladdin (P. R. China). All reagents were used as received without any further purification.

2.1 Synthesis of Bi_2MoO_6 nanosheets

In a typical procedure, 2 mmol of $Bi(NO_3)_3 \cdot 5H_2O$ was dissolved in 20 mL of nitric acid solution (2 mol L^{-1}) while stirring for 10 min. Next, 10 mL of Na_2MoO_4 solution (0.1 mol L^{-1}) was slowly added into the above solution under vigorous stirring. Then, pH of the solution was adjusted to 3 with $NH_3 \cdot H_2O$, after which the mixture was transferred to a 50 mL Teflon stainless-steel autoclave and heated at 180 °C for 24 h. The product was separated by centrifugation, washed with distilled water and ethanol several times and dried at 80 °C for 6 h.

2.2 Synthesis of Bi_2MoO_6 & Bi_2S_3 heterojunctions

Bi_2MoO_6 & Bi_2S_3 heterojunctions were synthesized through a facile anion exchange process starting from the obtained Bi_2MoO_6 nanosheets. First, the prepared Bi_2MoO_6 nanosheets (90 mg) and PVP (0.5 g) were dispersed in 20 mL of deionized water by sonication, and then, 20 mL of $Na_2S \cdot 9H_2O$ (0.072 mol L^{-1}) was dropped into the above mixture. After vigorous magnetic stirring for 20 min, the obtained mixture was transferred into a 50 mL Teflon-lined stainless-steel autoclave and kept at 150 °C in an electric oven. After naturally cooling the solution to room temperature, the final products were collected by centrifugation, washed and dried at 80 °C for 6 h. Specifically, the hydrothermal time was either 0.5 h, 1 h, 2 h, 4 h or 6 h during the above reaction, with the resulting samples labelled as BMO-S0.5, BMO-S1, BMO-S2, BMO-S4 and BMO-S6, respectively.

2.3 Microstructural characterization

X-ray diffraction (XRD) measurements were conducted on a Rigaku Ultima IV powder X-ray diffractometer using Cu Kα radiation (λ = 1.54 Å) with a scanning speed of 0.2° min^{-1}. Field emission scanning electron microscopy (FESEM, JSM-7500F, operating accelerating voltage of 20 kV) was used to analyse the morphologies and structures of synthesized samples. Energy dispersive spectroscopy (EDS) was used to identify the

Published on 16 October 2018. Downloaded by California State University at Long Beach on 6/7/2019 2:09:54 AM.

chemical composition at 10 kV accelerating voltage. Transmission electron microscopy (TEM) measurements were conducted on a Tecnai G2 F20 S-TWIN with a field emission gun at 20 kV. ICP-AES (Agilent 720) was used to determine the relative contents of Bi_2S_3 and Bi_2MoO_6 in the heterojunctions. Moreover, X-ray photoelectron spectroscopy (XPS) was carried out on an ESCALAB 250 X-ray instrument using monochromatic Al Kα radiation. Specific surface areas and pore size distributions were calculated by the Brunauer–Emmett–Teller (BET) and Barrett–Joyner–Halenda (BJH) methods using nitrogen adsorption isotherms measured on a MicrotracBEL BELSORP-max. UV-vis diffuse reflection spectroscopy (DRS) was performed on a Shimadzu UV-vis 2550 spectrophotometer (UV-vis, Japan). Photoluminescence (PL) spectra were measured at room temperature using a F97 Pro fluorescence spectrometer. Transient photocurrents, electrochemical impedance spectroscopy (EIS) and Mott–Schottky (M–S) measurements were performed with a standard three-electrode system on an electrochemical workstation (CHI 660e). The light source was a 300 W Xe lamp, and the electrolyte was a 0.5 M Na_2SO_4 solution.

2.4 Adsorption experiment

Selective adsorption experiments for various pollutants, including RhB, MO, AF, MB, CIP, SF and Cr(VI) solution, were performed on the prepared materials. Detailed adsorption experiments are shown in the ESI.†

2.5 Photocatalytic test

Photocatalytic activities for Cr(VI) reduction were evaluated for the prepared samples under a simulated visible-light source with 500 W Xe lamp filtered by a 420 nm cut-off. In a typical process, 20 mg of the sample was added to 50 mL of Cr(VI) solution (20 mg L^{-1}) and stirred for 80 min in dark to reach the adsorption–desorption equilibrium. After stopping visible light illumination, the concentration of Cr(VI) in sample was analysed at the maximum absorption peak of 540 nm [9,35] at specific time intervals. Regeneration of the BMO-S1 heterojunction was conducted between each adsorption of 50 mL Cr(VI) solutions (20 mg L^{-1}).

3. Results and discussion

3.1 Structure analysis

The evolution of phase structures of the prepared products was investigated based on time-dependent experiments, and the corresponding XRD patterns are shown in Fig. 1. For pure Bi_2MoO_6, diffraction peaks at 28.27°, 32.47°, 33.15°, 47.21° and 55.61° can be indexed to the (131), (002), (260), (210), and (331) planes of orthorhombic Bi_2MoO_6 (JCPDS file no. 77-1246, a = 5.5 Å, b = 16.24 Å, c = 5.49 Å), respectively. No peaks of impurities are observed. After a 0.5 h hydrothermal reaction (BMO-S0.5), the diffraction peak intensities of Bi_2MoO_6 declined slightly. With the reaction time prolonged to 1 h (BMO-S1), new peaks at 2θ = 25.21°, 28.64° and 31.81° appeared, which can be respectively assigned to the (031), (023) and (122) planes of orthorhombic Bi_2S_3 (JCPDS file no. 84-0279, a = 11.147 Å, b = 11.305 Å, c = 3.981 Å). Meanwhile, the diffraction peak intensities of Bi_2MoO_6 reduced further. As the reaction time was further extended to 2 h, the peaks of Bi_2MoO_6 almost disappeared, and with even more prolonged reaction time, no peaks of Bi_2MoO_6 can be distinguished in the sample, indicating that pure Bi_2S_3 was obtained. XRD analysis indicates the transformation from Bi_2MoO_6 to Bi_2S_3 and a co-existence of the two components in the prepared BMO-S1 sample.

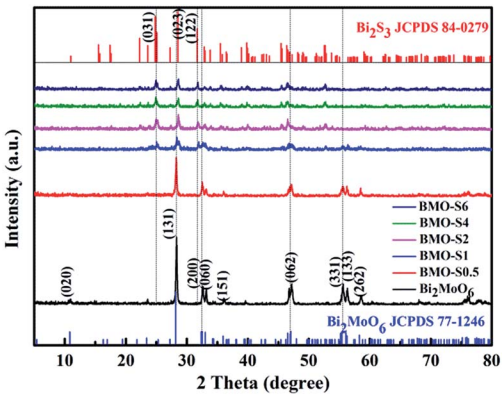

Fig. 1 XRD patterns of all prepared samples.

Surface chemical states and compositions of Bi_2MoO_6, BMO-S1 and BMO-S6 (Bi_2S_3) were elucidated by XPS analysis, as shown in Fig. 2a. Here, all peaks can be indexed to Bi, Mo, S, O, and C elements. C 1s (284.6 eV) spectrum was used as a reference to calculate the binding energies of other elements. Fig. 2b shows the typical high resolution XPS spectra of Mo 3d. For bare Bi_2MoO_6, two peaks located at 236.1 and 233.2 eV can be assigned to the Mo $3d_{3/2}$ and Mo $3d_{5/2}$ spin states of Mo^{6+} in Bi_2MoO_6,[36] respectively. Obviously, the peak of Mo decreased greatly as the reaction time was extended, illustrating a decrease in Mo content in the samples. Also of note is that the Mo^{6+} peaks of BMO-S1 sample obviously shift to lower binding energies compared with that of pure Bi_2MoO_6, which may be caused by a strong interaction between Bi_2S_3 and Bi_2MoO_6. No signals of Mo can be detected for BMO-S6 (Bi_2S_3) sample,

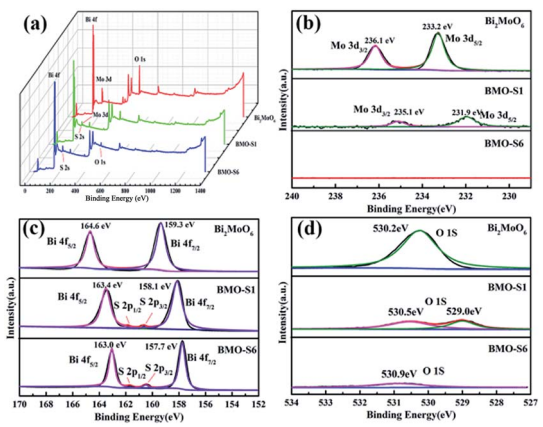

Fig. 2 XPS spectra of Bi_2MoO_6, BMO-S1 and BMO-S6 (Bi_2S_3). (a) Survey scan, (b) Mo 3d spectra, (c) Bi 4f spectra and (d) O 1s spectra.

This journal is © The Royal Society of Chemistry 2018

Published on 16 October 2018. Downloaded by California State University at Long Beach on 6/7/2019 2:09:54 AM.

further indicating that no Bi_2MoO_6 is left in the sample and thereby, confirming XRD results. In Fig. 2c, peaks at binding energies of 159.3 and 164.6 eV can be assigned to Bi $4f_{7/2}$ and Bi $4f_{5/2}$ of Bi^{3+} in Bi_2MoO_6, respectively.[16,37,38] For BMO-S6 (Bi_2S_3), two peaks present at 157.7 eV and 163 eV are attributed to Bi $4f_{7/2}$ and Bi $4f_{5/2}$,[39] suggesting the existence of Bi^{3+} from the Bi_2S_3. The resulting binding energies of Bi 4f peaks in the BMO-S1 heterojunction appear in a lower energy region than in the pure Bi_2MoO_6, originating from the electrons transfer between Bi_2S_3 and Bi_2MoO_6 in the heterojunction. Moreover, peak intensities of the Bi element are almost unchanged, illustrating a complete conversion from Bi_2MoO_6 to Bi_2S_3. Finally, Fig. 2d depicts the spectra for O 1s. The peak at binding energy of 530.2 eV is attributed to the binding energy of normal lattice oxygen in Bi_2MoO_6.[16,38] The O 1s spectrum of BMO-S1 could be deconvoluted into two Gaussian peaks, including a lower energy peak at 529 eV, corresponding to lattice oxygen, and a higher energy peak at 530.5 eV, consistent with surface adsorbed oxygen from the atmosphere. For BMO-S6 (Bi_2S_3) sample, the peak at 530.9 eV is related to surface hydroxyl groups (O–H).[17] Notably, the peaks of Mo 3d, Bi 4f and O 1s for BMO-S1 exhibit obvious shifts compared with pure Bi_2MoO_6, which could be attributed to the strong interaction between Bi_2MoO_6 and Bi_2S_3 formed during *in situ* sulfuration process.

To understand the *in situ* reaction process, the Bi_2MoO_6 & Bi_2S_3 heterojunctions synthesized at different reaction times were characterized by SEM. Fig. 3a shows that the pure Bi_2MoO_6 sample exhibits a uniform sheet-shaped structure with a smooth surface and an average width of 100–200 nm. At the initial reaction stage (0.5 h), geometry of the sample remains the same, but the surfaces are fuzzier, indicating the formation of Bi_2S_3 thin layer on the surface of Bi_2MoO_6. As reaction time extends to 1 h, a transformation in the structure occurs from thick nanosheets to much thinner layers with Bi_2S_3 capped Bi_2MoO_6. After a reaction time of 2 h, the BMO-S2 sample exhibits a stub shape, which is very similar to the structure of Bi_2MoO_6. Further prolonging the reaction time to 4 h and 6 h, the samples remain mainly composed of nanostubs without obvious differences. We can conclude that during the reaction, Bi_2MoO_6 nanosheets *in situ* transformed into Bi_2S_3 due to their similarly layered structures and common Bi element. Moreover, the distributions of individual elements over BMO-S1 sample have been characterized using EDS elemental mapping technique. EDS results in Fig. S1† confirm a uniform distribution of Bi, Mo, O and S elements throughout the Bi_2MoO_6 & Bi_2S_3 heterojunctions.

More detailed structural information of the bare Bi_2MoO_6, BMO-S1 and BMO-S6 (Bi_2S_3) samples have been provided by TEM and HRTEM analysis, as shown in Fig. 4. From Fig. 4a, we see that well-defined Bi_2MoO_6 nanosheets with smooth, distinct faces are formed, which is consistent with SEM observation in Fig. 3a. The resolved lattice fringes of 0.270 and 0.275 nm in Fig. 4b correspond to (060) and (200) planes of orthorhombic Bi_2MoO_6, respectively, which are perpendicular to the (001) facet. The corresponding Fast Fourier Transform (FFT) shown inset in Fig. 4a further affirms the single crystal structure of the prepared Bi_2MoO_6 with diffraction spots that are consistent with HRTEM results. The TEM image of BMO-S1 in Fig. 4c reveals that the Bi_2S_3 thin layer wraps around the sheet-like Bi_2MoO_6, indicating the formation of a core–shell structure. From HRTEM image in Fig. 4d, we clearly see the boundary region between Bi_2MoO_6 and Bi_2S_3 with obvious lattice disorder, which is caused by the mismatch of crystal lattices. Two sets of lattice fringes with spacings of 0.32 nm and 0.28 nm,

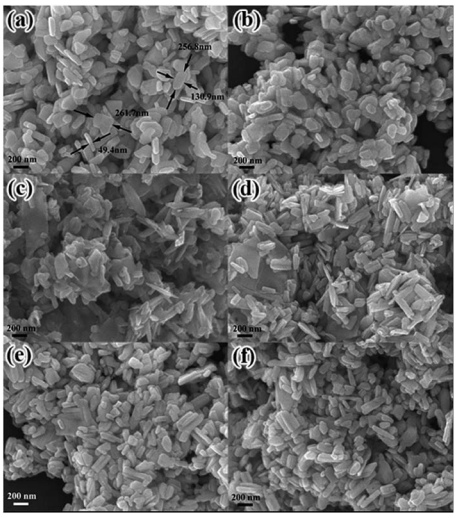

Fig. 3 SEM images of (a) Bi_2MoO_6, (b) BMO-S0.5, (c) BMO-S1, (d) BMO-S2, (e) BMO-S4 and (f) BMO-S6 (Bi_2S_3).

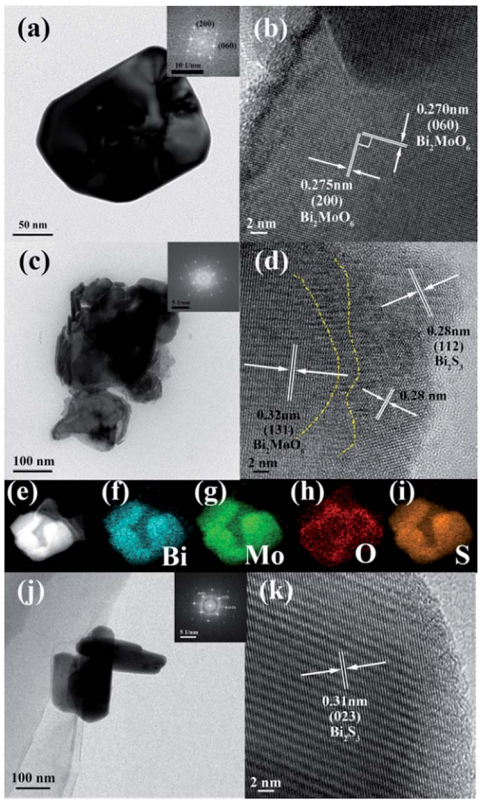

Fig. 4 TEM and HRTEM images of (a and b) Bi_2MoO_6, (c and d) BMO-S1 and (j and k) BMO-S6 (Bi_2S_3). STEM image (e) and elemental mapping for (f) Bi, (g) Mo, (h) O, and (i) S elements in BMO-S1.

Published on 16 October 2018. Downloaded by California State University at Long Beach on 6/7/2019 2:09:54 AM.

corresponding to (131) crystal plane of orthorhombic Bi_2MoO_6, and (112) plane of Bi_2S_3, respectively, are observed indicating the formation of a heterojunction. In addition, EDS results in Fig. S2† reveal that the elements in BMO-S1 are mainly O, Bi, Mo, and S. Elemental mapping of BMO-S1 shown in Fig. 4e–i further illustrate the uniform spatial distribution of Bi_2S_3 over Bi_2MoO_6. As for BMO-S6 (Bi_2S_3), only nanorods are observed. FFT shown inset in Fig. 4j indicates the single crystalline structure of Bi_2S_3 nanorods. The corresponding HRTEM image is shown in Fig. 4k, where interplanar spacing of 0.31 nm corresponds to the (023) lattice plane of orthorhombic Bi_2S_3.

Quantitative chemical composition of the Bi_2MoO_6 & Bi_2S_3 heterojunctions were determined by ICP-AES and the results are shown in Table 1. Clearly, the mass percentage of Bi_2S_3 in heterojunctions increases while that of Bi_2MoO_6 decreases with the extension of reaction time. For BMO-S1, the mass percentage of Bi_2S_3 is 47.27 wt%. As the reaction time is prolonged to 6 h (BMO-S6), all Bi_2WO_6 is quantitatively sulfurated into Bi_2S_3 and the results agree with XRD and XPS analysis.

The above results suggest that Bi_2MoO_6 & Bi_2S_3 heterojunctions with core–shell structure can be successfully prepared through a facile *in situ* anion exchange process. In this procedure, Bi_2MoO_6 could be easily converted into Bi_2S_3 in the presence of S^{2-} ions due to the extremely low solubility of Bi_2S_3 ($K_{sp} = 1 \times 10^{-97}$).[40] Thus, the surface of Bi_2MoO_6 nanosheets was first etched to generate Bi_2S_3 nanocrystals, which grew into thin layers coated on the Bi_2MoO_6 nanosheets as the reaction time was prolonged. Furthermore, the similarly layered structures of Bi_2MoO_6 and Bi_2S_3 favour the anion exchange and facilitate the formation of Bi_2MoO_6 & Bi_2S_3 heterojunctions. Therefore, an intimate core–shell junction was formed between Bi_2MoO_6 and Bi_2S_3, which can promote charge separation and efficient carrier transfer, and hence achieve a higher photocatalytic activity in the heterojunction.

Fig. 5 shows the nitrogen adsorption–desorption isotherms of Bi_2MoO_6 and Bi_2MoO_6 & Bi_2S_3 heterojunctions. All isotherms show type IV behaviour with H3 hysteresis loops at high P/P_0, indicating a mesoporous structure (2–50 nm). The Brunauer–Emmett–Teller (BET) specific surface areas of all samples are summarized in Table S1.† Notably, the BET surface areas of Bi_2MoO_6 & Bi_2S_3 heterojunctions first increase and then decrease with increased reaction time and BMO-S1 sample shows the highest surface area at 26.865 $m^2\ g^{-1}$. The pore size distribution curves (inset in Fig. 5) estimated from the adsorption branches using the Barrett–Joyner–Halenda (BJH) method exhibit wide pore size distributions from 2 to 100 nm,

Table 1 Bi_2MoO_6 and Bi_2S_3 content of the samples as determined by ICP-OES

Samples	Bi_2MoO_6 (wt%)	Bi_2S_3 (wt%)
Bi_2MoO_6	100	0
BMO-S0.5	90.18	9.82
BMO-S1	52.73	47.27
BMO-S2	3.13	96.87
BMO-S4	0.11	99.89
BMO-S6 (Bi_2S_3)	0	100

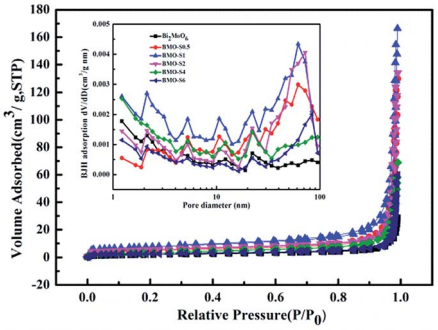

Fig. 5 N_2 adsorption–desorption isotherms and pore size distribution curves (inset) of all samples.

illustrating the presence of mesoporous and microporous structures. Moreover, the mean pore diameters and cumulative pore volumes of Bi_2MoO_6 & Bi_2S_3 heterojunctions listed in Table S1† have the same trend as the surface area, with BMO-S1 heterojunction exhibiting maximum values of 0.26 nm and 43.1 $cm^3\ g^{-1}$, respectively. Furthermore, Bi_2MoO_6 & Bi_2S_3 heterojunctions display multimodal pore-size distributions with a maximum pore diameter of 65 nm, while only mesopores are observed for Bi_2MoO_6. The porous structure of Bi_2MoO_6 & Bi_2S_3 heterojunctions will aid the degradation of pollutants by facilitating adsorption and diffusion of molecules.

3.2 Adsorption/photocatalytic reduction of Cr(VI)

To reveal adsorption performance of the core–shell Bi_2MoO_6 & Bi_2S_3 heterojunctions, several environmental pollutions, including MB, MO, AF, RhB, CIP, SF and Cr(VI), have been employed as targets. Adsorption behaviour of BMO-S1 towards various contaminants was examined by determining the change in their characteristic absorption peaks (Fig. S3†). BMO-S1 exhibits distinct selective adsorption towards Cr(VI). The systematic investigation into adsorption performance of BMO-S1 suggests that the adsorption of Cr(VI) onto BMO-S1 can be well-fitted by a pseudo-second-order kinetic model (Fig. S4†), indicating chemisorption of Cr(VI).[25,26,41] Moreover, the selective adsorption for Cr(VI) will promote photocatalytic Cr(VI) reduction.

To demonstrate photocatalytic reduction of Cr(VI) to Cr(III) on these Bi_2MoO_6 & Bi_2S_3 heterojunctions, UV-vis spectroscopy of Cr(VI) at different time intervals was carried out under visible light irradiation ($\lambda > 420$ nm), as shown in Fig. S5.† Characteristic absorption peak at 542 nm gradually decreases with prolonged irradiation time for all samples, revealing photocatalytic reduction of Cr(VI). The reduction of Cr(VI) as a function of time for all tested catalysts is shown in Fig. 6a. All Bi_2MoO_6 & Bi_2S_3 heterojunctions show remarkably higher reduction activity than either of the single-component samples. Interestingly, BMO-S1 (47.27 wt% of Bi_2S_3) catalyst exhibits the highest photocatalytic activity with a reduction rate of 100% within 16 min, while only 13% and 60% of Cr^{6+} reduction is achieved over bare Bi_2MoO_6 and BMO-S6 (Bi_2S_3), respectively, within 25 min (Fig. 6a). Moreover, the content of Bi_2S_3 is also observed to have a significant

 This journal is © The Royal Society of Chemistry 2018

Published on 16 October 2018. Downloaded by California State University at Long Beach on 6/7/2019 2:09:54 AM.

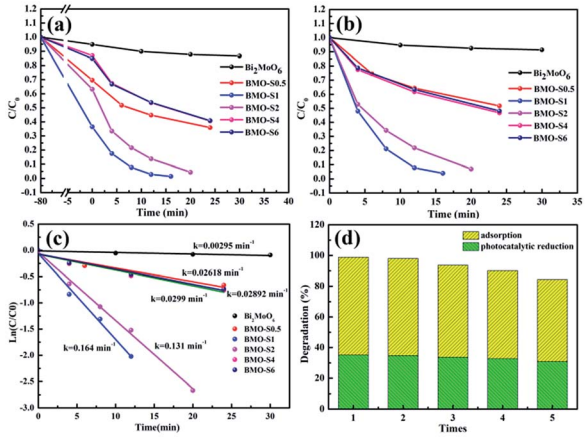

Fig. 6 (a) Adsorption in dark and photocatalytic reduction of Cr(VI) over different samples. (b) Normalized photocatalytic reduction of Cr(VI) under simulated solar light. (c) Plots of $\ln(C/C_0)$ *versus* time for Cr(VI) reduction over various catalysts. (d) Stability of BMO-S1 within five consecutive cycles.

impact on adsorption and photocatalytic reduction performance. Both adsorption and photocatalytic reduction activity of Bi_2MoO_6 & Bi_2S_3 increase remarkably with increasing amount of Bi_2S_3 and then decrease with excess amount of Bi_2S_3. Excess Bi_2S_3 content may reduce the amount of photo-generated charges due to unfavourable morphology and poor charge transport in Bi_2S_3,[21] leading to a slight decrease in Cr(VI) reduction efficiency. Notably, adsorption of Cr(VI) onto BMO-S1 is approximately 10 and 6 times higher than that on Bi_2MoO_6 and BMO-S6 (Bi_2S_3), respectively. Considering that the photocatalytic reduction reaction mainly occurs on the surface of catalysts, the greatly enhanced adsorption of Cr(VI) molecules also contributes to the excellent photocatalytic reduction activity of Bi_2MoO_6 & Bi_2S_3 heterojunctions.

Interestingly, BMO-S1 catalyst displays the best photocatalytic activity for Cr(VI) reduction regardless of adsorption considerations (Fig. 6b). To quantitatively understand the reaction kinetics of Cr(VI) reduction over BMO-S1, pseudo-first-order kinetics of Langmuir–Hinshelwood (eqn (1)) is applied.

$$-\ln\frac{C}{C_0} = kt \quad (1)$$

where, C_0 and C are the concentrations of Cr(VI) in solution at initial time t_0 and t, respectively, and k is the apparent first-order rate constant.

Corresponding plots of $\ln(C/C_0)$ *versus* time are shown in Fig. 6c, the observed good linear correlations indicate the Cr(VI) reduction follows first-order kinetics.[23] All Bi_2MoO_6 & Bi_2S_3 heterojunctions show higher Cr(VI) reduction rates than pure Bi_2MoO_6 and Bi_2S_3 (BMO-S6). The highest apparent rate constant of $k = 0.164\ min^{-1}$ is obtained for BMO-S1 photocatalyst, which is about 55 and 5.7 times that of bare Bi_2MoO_6 ($0.00295\ min^{-1}$) and Bi_2S_3 ($0.02892\ min^{-1}$), respectively. Thus, the core–shell Bi_2MoO_6 & Bi_2S_3 heterojunctions exhibit dramatically enhanced photocatalytic reduction Cr(VI).

Apart from the remarkable Cr(VI) reduction efficiency, the stability of photocatalysts is also an important factor in practical applications. Therefore, we conducted recycling experiments for the reduction of Cr(VI) over BMO-S1 heterojunction under visible light irradiation. As illustrated in Fig. 6d, BMO-S1 shows adequate cyclic stability, maintaining 90% of initial activity after five successive catalytic runs. Notably, the gradually decreased removal efficiency is mainly caused by decreased adsorption capacity while no significant changes in photocatalytic reduction activity are seen. The slight decrease in adsorption capacity might be due to incomplete desorption of Cr(III) and loss of BMO-S1 during separation and washing processes.[42] Moreover, XRD pattern of BMO-S1 after five successive catalytic runs in Fig. S6† confirms the high stability of BMO-S1 heterojunction.

To highlight the advantages of our core–shell Bi_2MoO_6 & Bi_2S_3 photocatalyst, a comparison of Cr(VI) reductions over various photocatalysts are listed in Table 2. The apparent rate constant of BMO-S1 catalyst is among the highest reported values of semiconductor photocatalysts for Cr(VI) reduction. Considering these results, the efficient and stable Bi_2MoO_6 & Bi_2S_3 heterojunctions from our current work can be used as promising photocatalysts for the reduction of Cr(VI) in industrial applications.

3.3 The mechanism for the enhanced photocatalytic activity of Bi_2MoO_6 & Bi_2S_3 heterojunctions

To investigate the mechanism of enhanced photocatalytic activity of Bi_2MoO_6 & Bi_2S_3 heterojunctions, UV-vis DRS, PL spectra, transient photocurrent responses and electrochemical impedance spectroscopy (EIS) of samples were studied. Fig. 7a displays the UV-vis DRS of pure Bi_2MoO_6, BMO-S1 and BMO-S6 (Bi_2S_3) samples. Notably, the light absorption ability of BMO-S1 heterojunction is greatly improved in nearly the entire visible light region, indicating more efficient utilization of visible light. The colour change in the three samples from faint yellow to dark brown and finally to ash black also indicates enhanced visible light absorption (Fig. 7a). Energy band gaps (E_g) were determined from the plots of $(F(Ra)hv)^2$ *versus* photon energy (hv), where $F(Ra)$ is a Kubelka–Munk function and hv is the energy of incident photon.[17] Calculated E_g for Bi_2MoO_6 and BMO-S6 (Bi_2S_3) are 2.71 and 1.92 eV, respectively (Fig. S7†). Obviously, the small band gap and large absorption coefficient of Bi_2S_3 [22,58,59] greatly enhanced visible light absorption by the Bi_2MoO_6 & Bi_2S_3 heterojunction, making it an attractive photocatalyst for Cr(VI) reduction.

Fig. 7b shows the PL spectra of all samples. A strong intrinsic luminescence emission peak at 551 nm can be observed for pure Bi_2MoO_6,[19] and the PL emission intensity decreases dramatically for Bi_2MoO_6 & Bi_2S_3 heterojunctions—indicating much lower recombination rate of photo-induced electrons and holes. BMO-S1 exhibits the weakest intensity of all samples, further proving that its most effective separation efficiency of electrons and holes could contribute to its best photocatalytic activity.[60]

To further evaluate the charge carrier transport and separation efficiency of samples, transient photoelectric currents (PC) of Bi_2MoO_6, BMO-S1, and BMO-S6 (Bi_2S_3) photoanodes were investigated under solar simulator irradiation. As shown in

Published on 16 October 2018. Downloaded by California State University at Long Beach on 6/7/2019 2:09:54 AM.

Table 2 Comparison of various photocatalysts for catalytic reduction of Cr(VI)

Material	Catalyst concentration (g L^{-1})	Cr(VI) concentration	Adsorption and catalytic time	Reduction percentage (%)	Rate constant (k, min^{-1})	Ref.
OH–TiO_2	1	10 mg L^{-1}	30 min + 30 min	88	0.079	12
Bi_2S_3/MoS_2	0.25	5 mg L^{-1}	60 min + 30 min	95	—	43
$BiVO_4/Bi_2S_3$	0.5	10 mg L^{-1}	10 min + 60 min	91.2	—	21
SnS_2/SnO_2	1	150 mg L^{-1}	60 min + 60 min	99	—	44
Bi_2S_3/C_3N_4	1	120 mg L^{-1}	60 min + 60 min	90	0.022	45
$BiVO_4$	0.5	10 mg L^{-1}	60 min + 80 min	95.3	—	46
$BiVO_4/MoS_2$	0.4	15 mg L^{-1}	60 min + 90 min	76.5	—	47
SnS_2	1	2×10^{-4} M	900 min + 90 min	99	—	48
Fe–g-C_3N_4/MoS_2	0.6	20 ppm	30 min + 150 min	91.4	0.021	2
BN/BiOCl	0.8	10 mg L^{-1}	30 min + 150 min	91	—	49
AgCl/Ag/TaON	10	1×10^{-4} M	30 min + 180 min	99	—	50
Ni_3S_2–graphene	1	20 mg L^{-1}	30 min + 180 min	91	—	51
Ag–BiOCl	1	10 mg L^{-1}	60 min + 180 min	86	0.012	52
TiO_2–RGO	1	10 mg L^{-1}	30 min + 240 min	91	—	53
TiO_2/RGO	0.5	12 mg L^{-1}	120 min + 240 min	86.5	—	54
$SrTiO_3$	1	10 mg L^{-1}	60 min + 240 min	99	0.028	55
CdS/RGO	1	10 mg L^{-1}	30 min + 250 min	92	—	56
BMO-S1	**0.4**	**10 mg L^{-1}**	**80 min + 16 min**	**100**	**0.164**	**This work**
CdS–$ZnIn_2S_4$	1	50 mg L^{-1}	60 min + 30 min	100	0.179	57

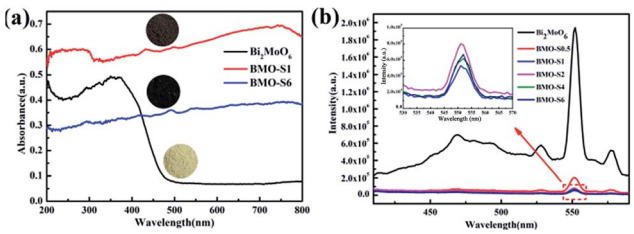

Fig. 7 (a) UV/vis diffuses reflectance spectra of Bi_2MoO_6, BMO-S1 and BMO-S6 (Bi_2S_3). (b) Room-temperature photoluminescence (PL) spectra of the prepared samples.

Fig. 8a, BMO-S1 shows the highest photocurrent response, which is about 25 times higher than that of pure Bi_2MoO_6 nanosheets. The high photocurrent density of BMO-S1 further indicates lowest recombination rate and improved separation efficiency of photo-generated electron–hole pairs.[61] Consequently, more electrons could be captured by Cr(VI) to form Cr(III). Electrochemical impedance spectroscopy (EIS) is an effective technology to study the charge transfer dynamics in interfacial regions.[62] Fig. 8b depicts the EIS changes between Bi_2MoO_6, BMO-S1, and BMO-S6 (Bi_2S_3). In general, a smaller arc in an EIS Nyquist plot indicates smaller charge-transfer resistance at the electrode surface.[63] Fig. 8b displays the relative arc radii of three electrodes in the order of BMO-S1 < BMO-S6 (Bi_2S_3) < Bi_2MoO_6. This result further confirms that the BMO-S1 heterojunction has highest separation efficiency of electron–hole pairs. Overall, PC and EIS results are consistent with PL analysis.

It is obvious that the generation and separation of electron–hole pairs is efficiently promoted by the Bi_2MoO_6 & Bi_2S_3 core–shell heterojunction under visible light irradiation. Mott–Schottky (M–S) measurements were conducted to further reveal the electronic structure of BMO-S1. The electrode potential *versus* reversible hydrogen electrode (RHE) was calculated according to Nernst equation (eqn (2)) and Mott–Schottky equation (eqn (3)):[64]

$$E_{RHE} = E_{SCE} + 0.059pH + E^0_{SCE} \quad (2)$$

$$c^{-2} = \frac{2}{e\varepsilon\varepsilon_0 N_d\left[E - E_{fb} - \frac{KT}{e}\right]} \quad (3)$$

where, E_{SCE} is the measured potential against Hg/Hg_2Cl_2/saturated KCl reference electrode. $E^0_{SCE} = 0.24$ V at pH 7, 25 °C. c is the capacitance of space charge layers. ε and ε_0 are the dielectric constant and the permittivity of vacuum, respectively. N_d is the carrier density of sample. E is the applied potential and E_{fb} is the flat band potential. K is the Boltzmann constant. T is the

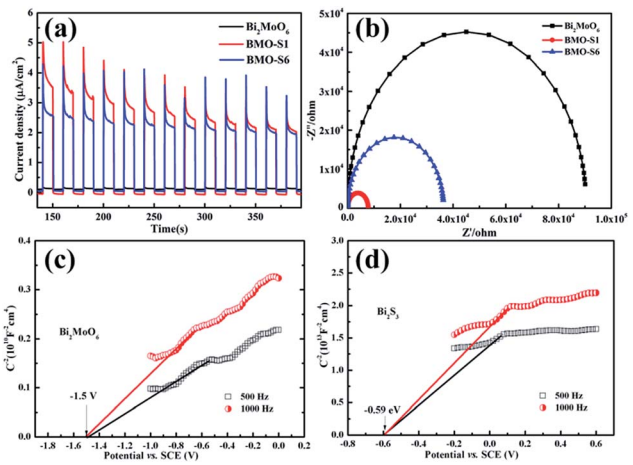

Fig. 8 (a) Transient photocurrent responses of Bi_2MoO_6, BMO-S1 and BMO-S6 (Bi_2S_3) under visible-light illumination. (b) Electrochemical impedance spectra (EIS) for Bi_2MoO_6, BMO-S1 and BMO-S6 (Bi_2S_3). (c and d) Mott–Schottky plots of Bi_2MoO_6 and BMO-S6 (Bi_2S_3).

This journal is © The Royal Society of Chemistry 2018

Published on 16 October 2018. Downloaded by California State University at Long Beach on 6/7/2019 2:09:54 AM.

absolute temperature, and e is the electron charge (1.602×10^{-19} C).

As shown in Fig. 8c and d, both Bi_2MoO_6 and Bi_2S_3 are n-type semiconductors due to the positive slopes of Mott–Schottky plots. Flat band potentials (E_{fb}) calculated from x intercept of the linear regions of these plots are −1.5 and −0.59 V (*vs.* Hg/Hg_2Cl_2, pH = 7) for Bi_2MoO_6 and BMO-S6 (Bi_2S_3), respectively. Generally, bottom of the conduction band of n-type semiconductor is near the flat band potential, which is dependent on the electron effective mass and carrier concentration.[65] Therefore, lower limits of conduction bands of Bi_2MoO_6 and Bi_2S_3 are about −1.5 and −0.59 V, respectively, which are equivalent to −1.26 and −0.35 V, respectively, *versus* a normal hydrogen electrode (E_{CB}). According to the empirical formula:

$$E_{VB} = E_{CB} + E_g \quad (4)$$

the calculated potentials of the top of VB for pure Bi_2MoO_6 and Bi_2S_3 are 1.45 and 1.57 V, respectively.

Based on all of the above analyses, the enhanced photocatalytic Cr(VI) reduction over Bi_2MoO_6 & Bi_2S_3 heterojunction is attributed to the combined effect of efficient separation of photo-generated electrons and holes, enhanced visible light absorption and strong adsorption ability for Cr(VI).

First, as can be seen from Fig. 9, the photo-generated electrons in CB of Bi_2MoO_6 (−1.26 eV) are enough to reduce O_2 and generate reactive oxygen species, such as $^{\bullet}O_2^-$, $^{\bullet}HO_2$, $^{\bullet}OH$ (eqn (5)–(9)):[66]

$$^{\bullet}O_2 + e^- \rightarrow {}^{\bullet}O_2^- \text{ (aq) } (E_0 = -0.33 \text{ V}) \quad (5)$$

$$O_2 + 2H_2O + 2e^- \rightarrow HO_2^- + OH^- \text{ (aq) } (E_0 = -0.065 \text{ V}) \quad (6)$$

$$O_2 + H^+ + e^- \rightarrow {}^{\bullet}HO_2 \text{ (aq) } (E_0 = -0.046 \text{ V}) \quad (7)$$

$$HO_2^- \text{ (aq)} + H_2O + e^- \rightarrow {}^{\bullet}HO \text{ (aq)} + OH^- \text{ (aq) } E_0 = 0.12 \text{ V}) \quad (8)$$

$$O_2 \text{ (g)} + 2H^+ + 2e^- \rightarrow H_2O_2 \text{ (aq) } (E_0 = 0.695 \text{ V}) \quad (9)$$

$$Cr_2O_7^{2-} + 14H^+ + 6e^- \rightarrow 2Cr^{3+} + 7H_2O \ (E_0 = 1.35 \text{ V}) \quad (10)$$

Although the reduction of Cr(VI) is thermodynamically favoured over that of reactive oxygen species (*i.e.*, E_0 = 1.36 V *vs.* NHE for eqn (2) and E_0 = −0.33 V *vs.* NHE for eqn (5)), the generation of superoxide reactive oxygen species cannot be omitted in air ambient. Since the reduction of Cr(VI) is mainly attributed to photo-induced electrons (e^-) in the CB, only a fraction of electrons could directly participate in the photocatalytic reaction for pure Bi_2MoO_6 and Bi_2S_3, leading to a low ability for Cr(VI) reduction. Meanwhile, rapid recombination of electrons and holes also reduces the reduction efficiency in the pure samples. When n-Bi_2MoO_6 and n-Bi_2S_3 come in contact with each other, type II heterojunction will form. As a result, the photo-generated electrons will flow from Bi_2MoO_6 core to Bi_2S_3 shell while the holes will migrate from Bi_2S_3 shell to Bi_2MoO_6 core due to matched band potentials, thus hindering the recombination of photo-induced electrons and holes. Moreover, due to the *in situ* formation of an intimate interface, the electron–hole pairs can be more efficiently separated in a shorter time. According to eqn (10), the electrons in CB of Bi_2S_3 (−0.35 eV *vs.* NHE) are negative enough to reduce the absorbed Cr(VI) on the surface of Bi_2S_3 to Cr(III) (E_0 = 1.35 V *vs.* NHE). Fortunately, electrons in the CB of Bi_2S_3 have similar redox potential as $O_2/{}^{\bullet}O_2^-$, and therefore, not negative enough to reduce O_2 to reactive oxygen species. Thus, the accumulated electrons could be utilized for effective Cr(VI) reduction. The transfers of electrons and holes not only help suppress the recombination of electron–hole pair, but also the consumption of electrons to form reactive oxygen species. Both effects could promote the photocatalytic activity of Bi_2MoO_6 & Bi_2S_3 heterojunction. As previously mentioned, the increased separation efficiency of charge carriers is the main reason for enhanced performance of BMO-S1. Meanwhile, the holes in VB of Bi_2MoO_6 (1.45 eV) are positive enough to oxidize OH^- in the solution (E_0 = 0.401 *vs.* NHE) in the absence of reducing agents (eqn (11)).

$$4OH^- \text{ (aq)} + 4h^+ \rightarrow O_2 + 2H_2O \quad (11)$$

It is generally recognized that photo-excited electrons play a key role in photocatalytic reduction of Cr(VI), however, quite a lot of reactive oxygen species are involved in the photocatalytic process.[67] To detect the effect of these reactive species on the photocatalytic reduction process for Cr(VI), an active species trapping experiments are conducted using edetic acid (EDTA) or oxalic acid (CA) as the h^+ scavengers, 1,4-benzoquinone (BQ) as $\cdot O_2^-$ scavenger, isopropanol (IPA) as ·OH scavenger and $KBrO_3$ as e^- scavenger. As shown in Fig. 10, photocatalytic Cr(VI) reduction was greatly accelerated by a dose of EDTA or CA, since EDTA and CA could greatly consume photo-generated holes, and promote separation efficiency of the photo-generated electrons and holes. Meanwhile, a slight decrease in degradation rate was observed when BQ was added, indicating $\cdot O_2^-$ plays a small role in the photocatalytic reduction process. Obviously, the reduction of Cr(VI) is suppressed with addition of $KBrO_3$, which may trap electrons and minimize their participation in the Cr(VI) reduction. However, upon the addition of IPA, photo reduction efficiency was decreased, suggesting that ·OH plays an important role in the photocatalytic reduction process. The standard redox potential of $\cdot OH/OH^-$ is 2.69 V *vs.* NHE, which is more positive than the VB position of Bi_2MoO_6 (1.45 eV). Thus, the photo-generated holes (h^+) cannot react

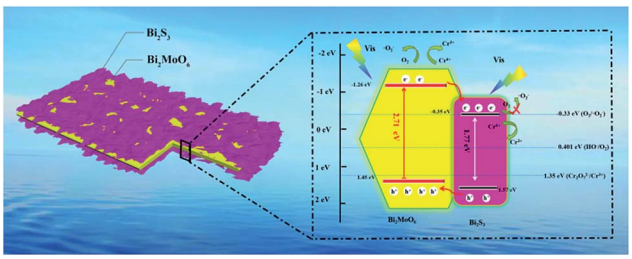

Fig. 9 Diagrams for energy levels and band structure of Bi_2MoO_6 & Bi_2S_3.

Published on 16 October 2018. Downloaded by California State University at Long Beach on 6/7/2019 2:09:54 AM.

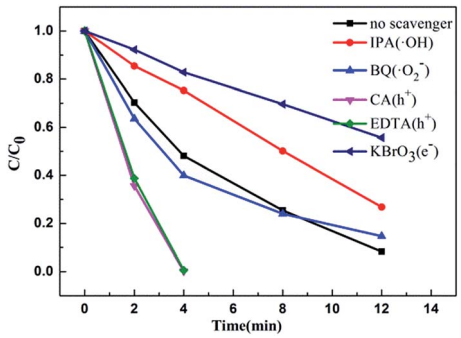

Fig. 10 Photocatalytic reduction efficiencies for Cr(VI) on Bi_2MoO_6 & Bi_2S_3 heterojunction in the presence of different scavengers under visible-light irradiation.

with H_2O to produce ·OH over Bi_2MoO_6. Therefore, ·OH is assumed to be produced *via* the following reactions:[68]

$$^{\cdot}O_2^- + H_2O \rightarrow {}^{\cdot}OOH + OH^- \quad (12)$$

$$^{\cdot}OOH + H_2O + 2e^- \rightarrow {}^{\cdot}OH + 2OH^- \quad (13)$$

The rapid consumption of ·OH by adding IPA will promote more electrons participating in the reduction of O_2 (eqn (5)), leading to lower efficiency for Cr(VI) reduction over the heterojunction.

Secondly, Bi_2S_3 can absorb full spectrum of sunlight, thereby, increasing the efficiency of a heterojunction for utilizing visible light and near-infrared region. Under visible light irradiation, considerably more electrons and holes can be generated and then separated effectively in the Bi_2MoO_6 & Bi_2S_3 heterojunction. Lastly, the selective chemical adsorption of Cr(VI), as well as higher specific surface area and numerous active sites, will facilitate more Cr(VI) adsorption on the surface of Bi_2MoO_6 & Bi_2S_3 heterojunction, which favours the subsequent photocatalytic reduction process. Thus, the core–shell Bi_2MoO_6 & Bi_2S_3 heterojunction structure in this work is confirmed to be a highly efficient photocatalyst for Cr(VI) reduction from wastewater.

4. Conclusions

In summary, 2D Bi_2MoO_6 & Bi_2S_3 heterojunctions were successfully constructed by an *in situ* anion exchange process. The prepared core–shell Bi_2MoO_6 & Bi_2S_3 heterojunctions with type II band structure and intimate interfaces aid the interfacial charge transfer driven by the staggered band gap structure under visible-light irradiation. The strong adsorption ability of Cr(VI) over the junction, increased surface area and enhanced visible light absorption contribute to the photocatalytic efficiency. As a result, the optimal Bi_2MoO_6 & Bi_2S_3 heterojunction exhibited a stable and extremely enhanced photocatalytic Cr(VI) reduction efficiency of $\kappa_{app} = 0.164\ min^{-1}$ in solution, which is 55 and 5.7 times that of bare Bi_2MoO_6 ($0.00295\ min^{-1}$) and Bi_2S_3 ($0.02892\ min^{-1}$), respectively.

Conflicts of interest

There are no conflicts to declare.

Acknowledgements

This work was financially supported by the NSF of China (No. 51502155, 51572152, 21673127 and 21671119), the Research Project of HPDE (No. D20151203), the State Key Laboratory of Structural Chemistry, FJIRSM (20170020) and The 111 Project of Hubei Province (2018-19-1).

References

1 S. Xu, H. Ding, S. Pan, Y. Luo and G. Li, *ACS Sustainable Chem. Eng.*, 2016, **4**, 6887–6893.
2 X. Wang, F. W. Zhang, Z. Y. Zhuang and Y. Yu, *ACS Sustainable Chem. Eng.*, 2016, **4**, 4055–4063.
3 B. Vellaichamy, P. Periakaruppan and B. Nagulan, *ACS Sustainable Chem. Eng.*, 2017, **5**, 9313–9324.
4 K. R. Zhu, X. L. Tan and C. L. Chen, *ACS Sustainable Chem. Eng.*, 2016, **4**, 4361–4369.
5 T. Zhou, C. Li, H. Jin, Y. Lian and W. Han, *ACS Appl. Mater. Interfaces*, 2017, **9**, 6030–6043.
6 K. Xiao, G. Han, J. Li, Z. Dan, F. Xu, L. Jiang and N. Duan, *RSC Adv.*, 2016, **6**, 5233–5239.
7 C. Lei, X. Zhu, B. Zhu, C. Jiang, Y. Le and J. Yu, *J. Hazard. Mater.*, 2017, **321**, 801–811.
8 W. Wang, B. Zhang, Q. Liu, P. Du, W. Liu and Z. He, *Environ. Sci.: Nano*, 2018, **5**, 730–739.
9 Y. Zhang, M. Xu, H. Li, H. Ge and Z. Bian, *Appl. Catal., B*, 2018, **226**, 213–219.
10 R. Zhao, B. L. Sun, Y. Z. Li, Y. M. Li, R. Yang and C. Wang, *J. Mater. Chem. A*, 2017, **5**, 1133–1144.
11 Z. Yu, X. Gao, Y. Yao, X. Zhang, G. Q. Bian, W. D. Wu, X. D. Chen, W. Li, C. Selomulya, Z. Wu and D. Zhao, *J. Mater. Chem. A*, 2018, **6**, 3954–3966.
12 Y. Li, Y. Bian, H. Qin, Y. Zhang and Z. Bian, *Appl. Catal., B*, 2017, **206**, 293–299.
13 N. H. Kera, M. Bhaumik, K. Pillay, S. S. Ray and A. Maity, *J. Colloid Interface Sci.*, 2017, **503**, 214–228.
14 Y. Zhang and Y.-J. Xu, *RSC Adv.*, 2014, **4**, 2904–2910.
15 J. Jiang, K. Zhao, X. Xiao and L. Zhang, *J. Am. Chem. Soc.*, 2012, **134**, 4473–4476.
16 H. Li, J. Liu, W. Hou, N. Du, R. Zhang and X. Tao, *Appl. Catal., B*, 2014, **160–161**, 89–97.
17 C. Yu, Z. Wu, R. Liu, D. D. Dionysiou, K. Yang, C. Wang and H. Liu, *Appl. Catal., B*, 2017, **209**, 1–11.
18 Y. S. Xu and W. D. Zhang, *Appl. Catal., B*, 2013, **140–141**, 306–316.
19 J. Tian, P. Hao, N. Wei, H. Cui and H. Liu, *ACS Catal.*, 2015, **5**, 4530–4536.
20 Y. Chen, G. Tian, Y. Shi, Y. Xiao and H. Fu, *Appl. Catal., B*, 2015, **164**, 40–47.
21 X. Gao, H. B. Wu, L. Zheng, Y. Zhong, Y. Hu and X. W. Lou, *Angew. Chem., Int. Ed.*, 2014, **53**, 5917–5921.

 This journal is © The Royal Society of Chemistry 2018

Published on 16 October 2018. Downloaded by California State University at Long Beach on 6/7/2019 2:09:54 AM.

22 Z. Zhang, W. Wang, L. Wang and S. Sun, *ACS Appl. Mater. Interfaces*, 2012, **4**, 593–597.
23 M. Xing, B. Qiu, M. Du, Q. Zhu, L. Wang and J. Zhang, *Adv. Funct. Mater.*, 2017, 1702624.
24 X. Q. Qiao, Z. W. Zhang, D. F. Hou, Z. Y. Tian, D. S. Li and Q. C. Zhang, *Cryst. Growth Des.*, 2017, **17**, 3538–3547.
25 X. Q. Qiao, F. C. Hu, F. Y. Tian, D. F. Hou and D. S. Li, *RSC Adv.*, 2016, **6**, 11631–11636.
26 X. Qiao, F. Hu, D. Hou and D. Li, *Mater. Lett.*, 2016, **169**, 241–245.
27 Q. Xiang, F. Cheng and D. Lang, *ChemSusChem*, 2016, **9**, 996–1002.
28 Q. Li, B. Guo, J. Yu, J. Ran, B. Zhang, H. Yan and J. R. Gong, *J. Am. Chem. Soc.*, 2011, **133**, 10878–10884.
29 L. Zhang, B. Tian, F. Chen and J. Zhang, *Int. J. Hydrogen Energy*, 2012, **37**, 17060–17067.
30 A. K. Rath, M. Bernechea, L. Martinez and G. Konstantatos, *Adv. Mater.*, 2011, **23**, 3712–3717.
31 A. Helal, F. A. Harraz, A. A. Ismail, T. M. Sami and I. A. Ibrahim, *Appl. Catal., B*, 2017, **213**, 18–27.
32 K. Yao, W. Gong, Y. Hu, X. Liang, Q. Chen and L. Peng, *J. Phys. Chem. C*, 2008, **112**, 8721–8724.
33 A. A. Tahir, M. A. Ehsan, M. Mazhar, K. G. U. Wijayantha, M. Zeller and A. D. Hunter, *Chem. Mater.*, 2010, **22**, 5084–5092.
34 H. Bao, C. M. Li, X. Cui, Y. Gan, Q. Song and J. Guo, *Small*, 2008, **4**, 1125–1129.
35 D. Lu, P. Fang, W. Wu, J. Ding, L. Jiang, X. Zhao, C. Li, M. Yang, Y. Li and D. Wang, *Nanoscale*, 2017, **9**, 3231–3245.
36 X. Q. Qiao, Z. W. Zhang, D. F. Hou, D. Li, Y. Liu, Y. Q. Lan, J. Zhang, P. Feng and X. Bu, *ACS Sustainable Chem. Eng.*, 2018, **6**, 12375–12384.
37 K. Jing, J. Xiong, N. Qin, Y. Song, L. Li, Y. Yu, S. Liang and L. Wu, *Chem. Commun.*, 2017, **53**, 8604–8607.
38 J. Di, J. Xia, M. Ji, H. Li, H. Xu, H. Li and R. Chen, *Nanoscale*, 2015, **7**, 11433–11443.
39 M. Zhang, C. Shao, J. Mu, X. Huang, Z. Zhang, Z. Guo, P. Zhang and Y. Liu, *J. Mater. Chem.*, 2012, **22**, 577–584.
40 X. Yang, X. Wang and Z. Zhang, *Mater. Chem. Phys.*, 2006, **95**, 154–157.
41 Q. Xu, Y. Wang, L. Jin, Y. Wang and M. Qin, *J. Hazard. Mater.*, 2017, **339**, 91–99.
42 Y. T. Zhuang, T. T. Zhu, M. Ruan, Y. L. Yu and J. H. Wang, *J. Mater. Chem. A*, 2017, **5**, 3447–3455.
43 B. Weng, X. Zhang, N. Zhang, Z. R. Tang and Y. J. Xu, *Langmuir*, 2015, **31**, 4314–4322.
44 Y. C. Zhang, L. Yao, G. Zhang, D. D. Dionysiou, J. Li and X. Du, *Appl. Catal., B*, 2014, **144**, 730–738.
45 D. Chen, J. Fang, S. Lu, G. Zhou, W. Feng, F. Yang, Y. Chen and Z. Fang, *Appl. Surf. Sci.*, 2017, **426**, 427–436.
46 C. Lv, J. Sun, G. Chen, Y. Zhou, D. Li, Z. Wang and B. Zhao, *Appl. Catal., B*, 2017, **208**, 14–21.
47 W. Zhao, Y. Liu, Z. Wei, S. Yang, H. He and C. Sun, *Appl. Catal., B*, 2016, **185**, 242–252.
48 C. Mondal, M. Ganguly, J. Pal, A. Roy, J. Jana and T. Pal, *Langmuir*, 2014, **30**, 4157–4164.
49 H. Xu, Z. Wu, M. Ding and X. Gao, *Mater. Des.*, 2017, **114**, 129–138.
50 J. Hou, C. Yang, Z. Wang, Q. Ji, Y. Li, G. Huang, S. Jiao and H. Zhu, *Appl. Catal., B*, 2013, **142–143**, 579–589.
51 P. Hu, X. Liu, B. Liu, L. Li, W. Qin, H. Yu, S. Zhong, Y. Li, Z. Ren and M. Wang, *J. Colloid Interface Sci.*, 2017, **496**, 254–260.
52 H. Li and L. Zhang, *Nanoscale*, 2014, **6**, 7805–7810.
53 X. Liu, L. Pan, T. Lv, G. Zhu, T. Lu, Z. Sun and C. Sun, *RSC Adv.*, 2011, **1**, 1245.
54 Y. Zhao, D. Zhao, C. Chen and X. Wang, *J. Colloid Interface Sci.*, 2013, **405**, 211–217.
55 D. Yang, Y. Sun, Z. Tong, Y. Nan and Z. Jiang, *J. Hazard. Mater.*, 2016, **312**, 45–54.
56 X. Liu, L. Pan, T. Lv, G. Zhu, Z. Sun and C. Sun, *Chem. Commun.*, 2011, **47**, 11984–11986.
57 G. Zhang, D. Chen, N. Li, Q. Xu, H. Li, J. He and J. Lu, *Appl. Catal., B*, 2018, **232**, 164–174.
58 W. Xu, J. Fang, Y. Chen, S. Lu, G. Zhou, X. Zhu and Z. Fang, *Mater. Chem. Phys.*, 2015, **154**, 30–37.
59 M. R. Gao, S. H. Yu, J. Yuan, W. Zhang and M. Antonietti, *Angew. Chem., Int. Ed. Engl.*, 2016, **55**, 12812–12816.
60 J. Li, L. Cai, J. Shang, Y. Yu and L. Zhang, *Adv. Mater.*, 2016, **28**, 5.
61 S. Bai, X. Li, Q. Kong, R. Long, C. Wang, J. Jiang and Y. Xiong, *Adv. Mater.*, 2015, **27**, 3444–3452.
62 M. A. Mahadadalkar, S. W. Gosavi and B. B. Kale, *J. Mater. Chem. A*, 2018, **6**, 16064–16073.
63 F. Y. Tian, D. Hou, W. M. Zhang, X. Q. Qiao and D. S. Li, *Dalton Trans.*, 2017, **46**, 14107–14113.
64 J. Ke, J. Liu, H. Sun, H. Zhang, X. Duan, P. Liang, X. Li, M. O. Tade, S. Liu and S. Wang, *Appl. Catal., B*, 2017, **200**, 47–55.
65 Z. Dai, F. Qin, H. Zhao, F. Tian, Y. Liu and R. Chen, *Nanoscale*, 2015, **7**, 11991–11999.
66 X. Li, J. Yu and M. Jaroniec, *Chem. Soc. Rev.*, 2016, **45**, 2603–2636.
67 X. Bai, Y. Y. Du, X. Y. Hu, Y. D. He, C. L. He, E. Z. Liu and J. Fan, *Appl. Catal., B*, 2018, **239**, 204–213.
68 C. Y. Wang, Y. J. Zhang, W. K. Wang, D. N. Pei, G. X. Huang, J. J. Chen, X. Zhang and H. Q. Yu, *Appl. Catal., B*, 2018, **221**, 320–328.